Instability in a spatially periodic open flow

Michael F. Schatz,[a] Dwight Barkley,[b] and Harry L. Swinney[c]
Center for Nonlinear Dynamics and Department of Physics, The University of Texas at Austin, Austin, Texas 78712

Laboratory experiments and numerical computations are conducted for plane channel flow with a streamwise-periodic array of cylinders. Well-ordered, globally stable flow states emerge from primary and secondary instabilities, in contrast with other wall-bounded shear flows, where instability generally leads directly to turbulence. A two-dimensional flow resembling Tollmien–Schlichting waves arises from a primary instability at a critical value of the Reynolds number, $R_1 = 130$, more than 40 times smaller than for plane Poiseuille flow. The primary transition is shown to be a supercritical Hopf bifurcation arising from a *convective* instability. A numerical linear stability analysis is in quantitative agreement with the experimental observations, and a simple one-dimensional model captures essential features of the primary transition. The secondary flow loses stability at $R_2 \approx 160$ to a tertiary flow, with a standing wave structure along the streamwise direction and a preferred wave number in the spanwise direction. This three-dimensional flow remains stable for a range of R, even though the structures resemble the initial stages of the breakdown to turbulence typically displayed by wall-bounded shear flow. The results of a Floquet stability analysis for the onset of three-dimensional flow are in partial agreement with experiment. © *1995 American Institute of Physics.*

I. INTRODUCTION

The transition to turbulence in wall-bounded shear flows, like those in channels, pipes, and boundary layers, is a basic problem of both fundamental and practical importance. Such flows are called *open* because fluid passes across boundaries into and out of the system. The turbulent transition in these systems is strikingly abrupt: as the Reynolds number R is increased, instability leads to the sudden, unpredictable transition from a laminar state to turbulence. Because the resulting turbulent flow has a very large number of degrees of freedom, concepts from hydrodynamic stability and dynamical systems theory have had limited success in describing the onset of turbulence in open fluid flows.

As an example, consider plane channel flow. Linear-stability calculations[1] predict that the laminar state becomes unstable at a critical Reynolds number, $R_1 = 5772.22$. Experiments, however, display a snap-through transition to turbulence at a smaller value of R that depends sensitively on external disturbances[2,3] (typically $R \sim 1000$). Experimentally, there are no simple, stable states mediating the transition to turbulence, and numerically there are no known simple flow states below $R \sim 2900$ (for pressure-driven flow).[4-7] As a result, there is no universally accepted picture for the onset of turbulence in plane channel flow.

The situation is different for *closed flows*, where fluid is confined by system boundaries. Here the transition to turbulence is more completely understood. Two prototypical closed flows are Couette–Taylor flow between rotating cylinders and Rayleigh–Bénard convection. As the control parameter (Reynolds or Rayleigh number) is increased in these systems, the simple laminar or conductive state becomes unstable to complex flow patterns through a sequence of bifurcations. Each bifurcation leads to a state that is more complex than those preceding, and each state is stable over some range of control parameter. The flow becomes chaotic or weakly turbulent only after several (but finitely many) such bifurcations.[8] This measured progression toward turbulence has enabled many detailed, quantitative comparisons between theory and experiment, ranging from the primary instability through the onset of chaos.[9]

In this paper we examine an open shear flow in which instabilities yield *stable* secondary and tertiary flows. The flow geometry, shown in Fig. 1, is plane channel flow geometrically perturbed in the streamwise direction by the periodic placement of small cylinders near one channel wall. By examining this flow, which was originally studied by Karniadakis *et al.*,[10] we are able to understand the initial stages of the transition to complex dynamics in an open flow[11] and to make quantitative comparisons between experiment and numerical computations.

In Sec. II we review previous work on instabilities in spatially periodic channel flows and introduce the governing equations and scalings. Our experimental and numerical approaches to the problem are described in Secs. III and IV, respectively. The results for the primary instability are presented in Sec. V, and those for secondary instability are given in Sec. VI. Section VII contains the conclusions and suggestions for future work.

II. PRELIMINARIES

A. Previous work

In technological applications ranging from microelectronics to nuclear reactors, advective heat and mass transport

[a]E-mail: schatz@chaos.utexas.edu
[b]Permanent address: Nonlinear Systems Laboratory, Mathematics Institute, University of Warwick, Coventry CV4 7AL, England. e-mail: barkley@maths.warwick.ac.uk
[c]E-mail: swinney@chaos.utexas.edu
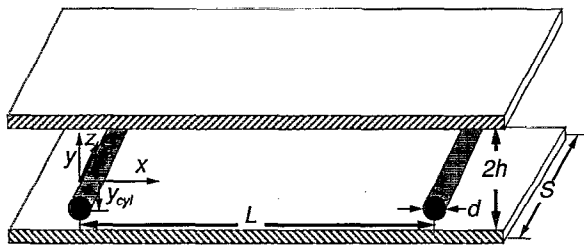
© 1995 American Institute of Physics

FIG. 1. Plane channel flow with spatially periodic perturbations in the streamwise direction, x.[10] Unless otherwise noted, x is referenced to the first cylinder (see Fig. 2), y to the channel half-height, and z to the center span. In units of the half-height h (0.794 cm in the experiment), the streamwise cylinder spacing is $L=6.66$, the cross-channel cylinder location is $y_{cyl}=-0.5$, and the cylinder diameter is $d=0.4$. In the experiment, the span $S=40$. In the stability computations, the span is assumed to be infinite.

FIG. 2. Schematic diagram of the channel flow experiment.

is commonly augmented by placing obstructions ("roughness elements" or "eddy promoters") in the flow domain.[10,12–16] The obstructions can induce instability in an otherwise laminar flow. Such unsteady laminar flows can provide good mixing with low dissipation, an attractive alternative to turbulent mixing, where pumping costs are higher and large shear stresses may threaten structural integrity (such as in blood oxygenators). The placement, size, and geometry of the obstructions are frequently determined empirically.

To model the effect of roughness elements on transport, previous channel flow experiments have been performed with geometric perturbations located periodically in the streamwise direction. In heat transfer studies on channel flows with spatially periodic triangular grooves, Greiner et al.[17] observed that enhanced heat transfer first occurs in downstream locations of the channel at $R \approx 200$ and moves upstream with increasing R; the unsteadiness was observed to be intermittent over a broad range of R. Similar observations have been reported by Stephanoff[13] for channel flow with two wavy walls. For the geometry of Fig. 1, Kozlu[18] observed the onset of unsteady flow for $R > 200$. There have been no previous experiments investigating details of hydrodynamic stability in spatially periodic channel flows.

Previous numerical simulations have investigated both primary and secondary transitions in spatially periodic channel flows. For two-dimensional (2-D) simulations of the geometry illustrated in Fig. 1, Karniadakis[19] presented evidence for a supercritical bifurcation to traveling waves at $R_1 \approx 150$. Furthermore, Karniadakis et al.[10] found that the spatial perturbations did not significantly alter the characteristic flow structures from those in plane channels—the dispersion relation and structure of the modes excited by the geometry in Fig. 1 compared well with those of Tollmien–Schlichting modes in plane channels. Amon and Patera[20] found similar results for the primary instability in a channel flow geometrically perturbed by rectangular grooves parallel to the z axis. They also studied the onset of three-dimensionality in this flow. From a temporal Floquet stability analysis of the fundamental spatial modes, they found that a 2-D traveling wave, which is stable over a range of R above the primary transition, undergoes a secondary instability
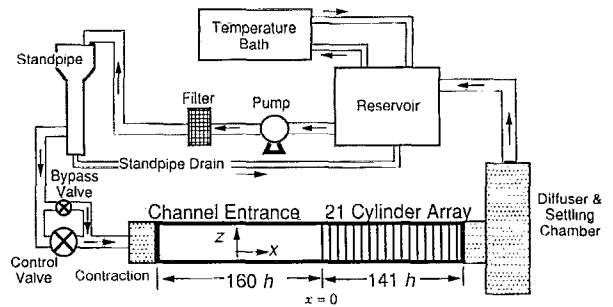
leading to a stable, ordered, three-dimensional (3-D) state. A phase portrait of this flow indicates that it is periodic in the laboratory frame.

B. Notation and scaling

Unless explicitly noted otherwise, all quantities will be presented in nondimensional form, as described in this section. The fluid flow in the spatially periodic channel is governed by the nondimensional incompressible Navier–Stokes equations:

$$\frac{\partial \mathbf{u}}{\partial t} + \mathbf{N}(\mathbf{u}) = -\nabla p + R^{-1} \nabla^2 \mathbf{u}, \tag{1}$$

$$\nabla \cdot \mathbf{u} = 0, \tag{2}$$

where $\mathbf{u}=(u,v,w)$ is the velocity and p is the static pressure. Here $\mathbf{N}(\mathbf{u})$ represents the nonlinear term:

$$\mathbf{N}(\mathbf{u}) = (\mathbf{u} \cdot \nabla)\mathbf{u}. \tag{3}$$

Lengths are scaled by the channel half-depth h (see Fig. 1). Because we will be considering flows in the spatially periodic channel driven under constant fluid flux conditions (see Sec. III A), the natural velocity scale is the centerline velocity U_{cl} of parabolic flow in a plane channel with the prescribed flux.[6,7] The velocity U_{cl} is measured directly in experiment, as described in the next section. In the numerical computations, we also consider constant flux conditions (see Sec. IV). The velocity scale is given by $U_{cl}=3Q/4h$, where Q is the flux per unit spanwise length through the channel $Q=\int_{-h}^{h} u \, dy$.[6,7] By fixing $Q=\frac{4}{3}$ and computing in a geometry with $h=1$, all quantities obtained from Eqs. (1)–(3) are properly scaled. The experimental Reynolds number is given by $R=hU_{cl}/\nu$, where ν is the kinematic viscosity of the working fluid (water). All other physical quantities are nondimensionalized in terms of these scales: time $t(h/U_{cl})$, wave number $k(1/h)$, frequency, and growth rate (U_{cl}/h).

III. EXPERIMENTAL SETUP

A. General features

The experiments are performed in a water channel with half-depth $h=0.794$ cm and span $S=31.75$ cm (see Fig. 1). Figure 2 shows a schematic diagram of the experimental setup. The test section, which contains an array of 21 cylinders, is 112 cm in length. Upstream of cylinder 1 (numbering from upstream to downstream) a channel entrance length of
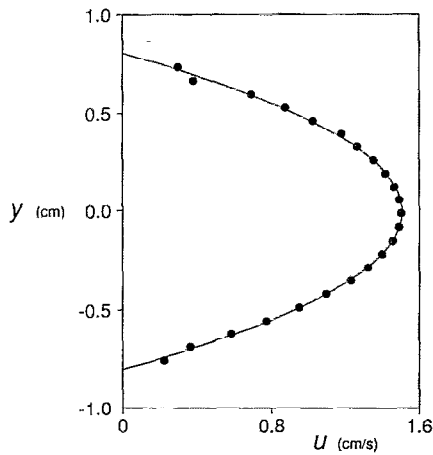
Phys. Fluids, Vol. 7, No. 2, February 1995

Schatz, Barkley, and Swinney   345

FIG. 3. Parabolic profile in the channel at $x = -10.4$, $z = -5.1$ (dimensionless units) at $R = 131.5$ for the experiment. The channel walls are located at $y = \pm 0.794$ cm. The curve is a parabolic fit to the experimental points.

FIG. 4. Velocity power spectrum at $R = 135$ from a hot film probe in the cylinder-array section at $x = 62.4$, $y = 0$, and $z = 13.6$. The integral of the spectrum is equal to the variance of the velocity time series.

127 cm ensures a fully developed plane Poiseuille flow for $R \lesssim 1400$.[21] The channel walls parallel to the x-z plane are constructed from glass plates of nominal 1.0 cm thickness. The glass walls are stiffened using aluminum ribs (5.7 cm $\times$ 5.7 cm cross section) attached to the center span of both channel walls. Variations in the channel wall spacing, determined using interferometry, are less than 2% overall and less than 1% in the region of the channel containing the cylinders. The cylinders are made from stainless steel that is centerless ground to a diameter $d = 0.3175 \pm 0.0004$ cm.

Fluid is continually recirculated through the channel. Water is pumped from a reservoir, through a 5 μm filter, and into a tall standpipe maintained at constant level by an overflow drain. The fluid is then metered to the experiment by a control valve. This arrangement maintains constant mass flux through the channel because the pressure drop across the control valve is much larger than that across the rest of the experiment. A ten to one 2-D contraction region with a matched cubic profile[22] reduces the background turbulence of flow into the channel entrance, while a diffuser provides a smooth transition from the channel exit to a settling chamber for the fluid. From the settling chamber, the fluid then drains back into the reservoir to repeat the cycle. A thermostatically controlled water bath regulates the temperature to ± 0.05 °C by directly circulating the working fluid through an independent flow loop. The section of the flow circuit from the control valve through the settling chamber is mounted on an optical table that pneumatically isolates the flow from mechanical vibrations.

Velocity and flow visualization measurements are conducted using a microcomputer based data acquisition system. Simultaneous measurements of streamwise velocity at different locations are obtained from two single-component forward scatter laser Doppler velocimetry (LDV) systems. A third LDV system monitors the laminar Poiseuille flow upstream of the cylinder array. Because the upstream flow is parabolic at the values of R we consider, the velocity scale U_{cl} is obtained directly from the upstream measurements. Figure 3 shows an upstream parabolic profile. Hot film
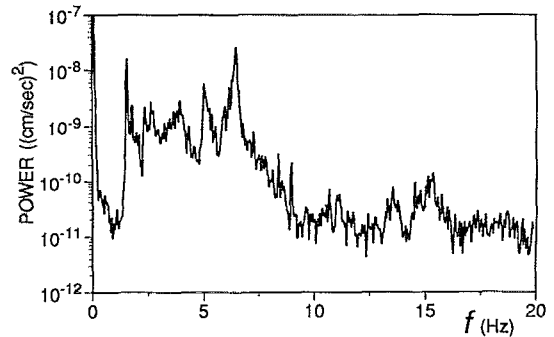
probes, calibrated *in situ* by LDV, yield a turbulent intensity of 0.07% (Fig. 4), which compares well with the 0.05% turbulence intensity obtained for channel experiments in wind tunnels.[3]

Electrochemical flow visualization is performed using the pH indicator thymol blue.[23] With the spatially periodic cylinders serving as electrodes, neutrally buoyant blue dye is produced near the cylinders, and is subsequently advected by the flow. Although the dye fronts are properly interpreted only as streaklines, information about the flow field (e.g., wavelength) can be obtained by observing the motion of the dye produced simultaneously at *different* cylinders. To increase the dye contrast, the flow is back-illuminated using sodium vapor lamps. A CCD video camera is used to view the flow; the video signal is recorded using a time lapse video recorder and is simultaneously digitized using a frame grabber. Digital image processing is performed to enhance and analyze the images.

B. Controlled disturbances

Controlled disturbances, often used to probe open flows,[3,24–26] are imposed in the experiment by two different methods: either by pulsing briefly the flow rate or by oscillating time periodically a foil inserted in the flow. The flow rate is pulsed by briefly opening for a time $\Delta t \approx 4$ (nondimensional) and then closing a bypass valve in parallel with the control valve (Fig. 2). Because the flow-rate change propagates through the channel as a pressure wave, the pulsed disturbance excites a step change in the entire flow simultaneously to within about 2 ms (the length of the experiment divided by the speed of sound in the fluid). During the flow-rate pulse, $u(y = 0)$ typically increases by 30%. With computer control, the triggering of the flow-rate pulses is synchronized with the acquisition of a velocity time series for each disturbance. This synchronization enables an impulsive disturbance to be identically repeated and recorded multiple times (typically 10–20) for fixed conditions. Greatly improved signal-to-noise ratios are obtained by averaging sets of time series.

Time-periodic disturbances are imposed by oscillating a foil inserted in the flow through a port located at $x = -4.8$. A schematic of the foil is shown in Fig. 5. The motion of the
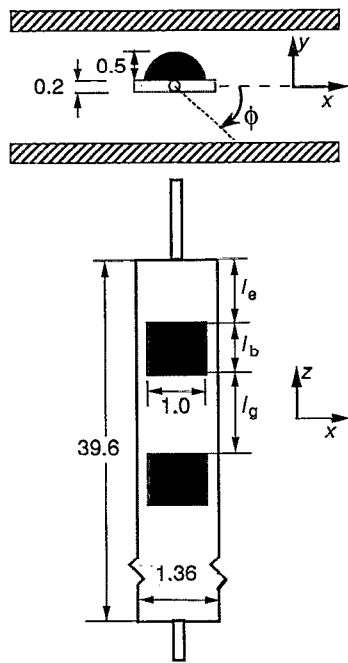
FIG. 5. End and side views of oscillating foil used to impose time-periodic disturbances at the inflow to the cylinder array. The protuberances extend a distance l_h in the z direction, and are separated by a distance l_g. See Table I for the sizes of l_e, l_b, and l_g.

foil does not change the flow rate through the channel. The foil oscillations, driven by direct coupling to a stepper motor, are symmetric about $y=0$ with angular amplitude ϕ; the angular velocity of the foil versus time is a square wave. The disturbance amplitude is increased by increasing ϕ with a fixed oscillation period. The foil position is continually monitored by a rotary shaft encoder with a resolution of better than $\pm 1°$.

The foil alone imposes 2-D disturbances in the channel flow. To impose 3-D disturbances, protuberances are mounted magnetically on one side of the foil, as shown in Fig. 5. By changing the placement and number of protuberances, 3-D disturbances of various initial spanwise wavelengths can be studied. The dimensions and placement of the protuberances for 3-D disturbances are listed in Table I.

TABLE I. Disturbance foil parameters. Unless otherwise noted, the foil oscillation frequency is fixed to 0.187 ± 0.003 and the angular amplitude ϕ is equal to $36°$ for both 2-D and 3-D time periodic disturbances.

No. of protuberances	l_e	l_b	l_g	$k_z^0 = 2\pi/(l_b+l_g)$
1	19.36	0.88	...	0.31[a]
2	11.86	0.88	14.12	0.42
4	7.22	0.88	7.22	0.78
5	5.87	0.88	5.87	0.90
6	4.90	0.88	4.90	1.09
8	3.62	0.88	3.62	1.40

[a]Computed by replacing l_g with l_e.

IV. NUMERICAL COMPUTATIONS

We have performed numerical linear-stability calculations of both steady and unsteady flows in the periodic channel geometry to compare with the experimental findings. In the steady-flow case, our stability computations provide a direct and accurate determination of the bifurcating frequency and of the critical Reynolds number R_1. For the unsteady (time-periodic) secondary flow, our computations provide an estimate of the critical spanwise wave number and critical Reynolds number R_2.

A. Time-dependent simulations

We use 2-D time-dependent simulations to obtain both the steady and time-periodic flow fields, whose stabilities are then investigated. The time-dependent simulations are carried out using a spectral-element program (PRISM) developed by Henderson at Princeton University.[27] In the spectral-element methodology the computational domain is divided into K elements, and within each element both the coordinates and solution variables (velocities and pressure) are approximated by Nth-order tensor-product polynomial expansions. A high-order time-splitting scheme is then used to time step the Navier–Stokes equations (1)–(3).[19,27–31]

In our computations the flow is assumed to be spatially periodic in the streamwise (x) direction; e.g., for 2-D flows $\mathbf{u}(x+nL,y,t)=\mathbf{u}(x,y,t)$, where L is the cylinder spacing and n is an integer determining the number of geometrical periods in the computational domain. The significance of assuming a periodic velocity field will become apparent in Sec. V. For all results reported, the number of spectral elements per geometrical period is fixed at 36. The polynomial expansions in our computations are typically of order $N=9$.

No-slip conditions on the velocity are imposed at the channel walls and at the cylinder surface. Since the pressure gradient ∇p, like the velocity $\mathbf{u}$, satisfies periodic boundary conditions in the streamwise direction, the pressure p must have the form $p(x,y,t)=p_0(x,y,t)+p_1(t)x$, where p_0 is the streamwise-periodic part of the pressure, $p_0(x+nL,y,t)=p_0(x,y,t)$, and p_1 is the streamwise-mean pressure gradient responsible for driving the flow. For constant-flux conditions (Secs. II B and III A) the mean pressure gradient p_1 is time dependent when the flow is unsteady. This requires that p_1 be computed at every time step, such that the flux be the prescribed constant value, $Q=\frac{4}{3}$.

To obtain the base flows needed for our stability computations, we simulate Eqs. (1)–(3) for a variety of Reynolds numbers in the range $100\leq R\leq180$. Initially at $R=100$ we start from a uniform state; thereafter, we use final conditions from one simulation as the initial conditions for the next. In all cases, the simulations are run for a time sufficient to obtain well-converged asymptotic states that are then stored for use in our stability computations. In the case of steady flows, this requires storing only the final flow field. In the case of time-periodic states, this requires the storing of a number of velocity fields (snapshots) over one time period. We find that 32 velocity fields equally spaced over one period are sufficient for representing the periodic flows, i.e., at intermediate times the flow field can be interpolated to well within the overall accuracy of the simulations.

B. Stability analysis

Let $U(x,y,t) = [U(x,y,t), V(x,y,t)]$ be a 2-D velocity field (steady or time periodic) whose stability is sought. An infinitesimal perturbation u' to this velocity field evolves according to the linearization of Eqs. (1)–(3):

$$\frac{d\mathbf{u}'}{dt} = -\mathbf{DN(U)u}' - \nabla p' + R^{-1}\nabla^2 \mathbf{u}', \qquad (4)$$

$$\nabla \cdot \mathbf{u}' = 0, \qquad (5)$$

where $\mathbf{DN(U)}$ is the (possibly time-periodic) linear operator:

$$\mathbf{DN(U)} \cdot \mathbf{u}' = (\mathbf{U} \cdot \nabla)\mathbf{u}' + (\mathbf{u}' \cdot \nabla)\mathbf{U} \qquad (6)$$

and p' is the perturbation to the pressure.

In the case of 2-D stability computations, the perturbation u' is itself 2-D: $u'(x,y,t) = u'(x,y,t) + v'(x,y,t)$. For our 3-D stability computations, we consider the geometry to be infinite in the spanwise direction z. Thus, it is sufficient to consider perturbations $\tilde{u}$ of the form

$$\mathbf{u}'(x,y,z,t) = \text{Re}[u'(x,y,t)e^{ik_z z}\hat{x} + v'(x,y,t)e^{ik_z z}\hat{y}$$
$$+ iw'(x,y,t)e^{ik_z z}\hat{z}], \qquad (7)$$

where k_z is the spanwise wave number of the perturbation. Because Eqs. (4)–(6) are linear in u', modes with different k_z do not couple; hence, we may treat k_z as a parameter and consider each k_z mode separately. Further details are given at the end of this section.

By defining $\mathbf{L(U)}$ to be the right-hand side of the linearized equations,

$$\mathbf{L(U)} \equiv -\mathbf{DN(U)u}' - \nabla p' + R^{-1}\nabla^2 \mathbf{u}', \qquad (8)$$

subject to the incompressibility constraint, we may write Eqs. (4)–(6) for the evolution of infinitesimal perturbations compactly as

$$\frac{\partial \mathbf{u}'}{\partial t} = \mathbf{L(U)} \cdot \mathbf{u}'. \qquad (9)$$

If $U = U(x,y)$ is a steady flow, then $\mathbf{L(U)}$ is a constant operator whose eigenvalues σ determine whether infinitesimal perturbations to U grow or decay: eigenvalues with a positive real part correspond to growing modes. If $U = U(x,y,t)$ is a time-periodic flow, then $\mathbf{L(U)}$ is also time periodic, and the stability of U is determined by the *Floquet multipliers* μ of this periodic operator. In this case, Floquet multipliers inside the unit circle in the complex plane correspond to decaying modes, and multipliers outside the unit circle correspond to growing modes.

The method used to find the relevant eigenvalues or multipliers is the same in both the steady and periodic cases. We define the operator $\mathbf{A}$ by

$$\mathbf{A(U)} \equiv \exp\left(\int_0^T \mathbf{L(U)}dt \right). \qquad (10)$$

Formally, $\mathbf{A}$ represents integration of the linear system (9) over time interval T, i.e., the operator $\mathbf{A}$ takes $u'(t=0)$ to $u'(t=T)$. In the case where U is time periodic, T is the period of the flow and $\mathbf{A}$ is equivalent to the linearized Poincaré map associated with the periodic orbit. The eigenvalues

of $\mathbf{A}$ are then precisely the Floquet multipliers μ. In the case where U is steady, T is chosen for computational convenience, but is otherwise arbitrary. In this case, it is more common to consider the exponents σ obtained from μ using the relation $\sigma = (\ln \mu)/T$.

From the operator $\mathbf{A}$ we find the eigenvalues of interest via subspace iteration starting from an initial Krylov subspace. Variations of the method have been used in other stability calculations.[20,32–36] We do not attempt to find all the eigenvalues of $\mathbf{A}$; we find only its dominant eigenvalues (those with the greatest magnitude), for these are the eigenvalues associated with instabilities. We use a Krylov space of dimension 8–20 and obtain converged eigenvalues with 20–40 iterations of the operator $\mathbf{A}$. Convergence varies considerably with the eigenvalue spectrum, however, and we have not always obtained a converged spectrum (see Sec. VI). The eigenvalues we report are accurate to better than 1%, which is sufficient for our purposes.

Application of the operator $\mathbf{A}$ [i.e., integration of (4)–(6)] requires two principal changes to the methods used to integrate Eqs. (1)–(3). First, we replace the nonlinear operator $\mathbf{N(U)}$ with the linear operator $\mathbf{DN(U)}$, where U is the velocity field obtained from time-dependent simulations. If U is time periodic, then $\mathbf{DN(U)}$ is obtained at any time t by interpolation from stored values of U at 32 times over one period. Second, for 3-D perturbations, the operator ∇ is replaced everywhere in Eqs. (4)–(6) by $(\nabla_2 + ik_z\hat{z})$, where ∇_2 is the 2-D gradient. This follows from the substitution of expression (7) for u' into the linearized Navier–Stokes equations. Thus, we only compute u' on a 2-D domain and treat k_z as a parameter.

V. PRIMARY INSTABILITY

In this section we present results showing that in the spatially periodic channel (1) the primary instability is strongly *convective* and no absolute instability appears, even with large increases in control parameter, and (2) the primary transition is *supercritical* and the resulting secondary flow is stable for a range of control parameter above onset.

A. Convective instability

The behavior at transition depends strongly on whether the instability is absolute or convective.[37] In the case of an absolutely unstable flow, virtually any small perturbation will eventually be amplified to the point where it will be observed as it fills the entire flow domain [Fig. 6(a)]. Even in cases where the nonlinear evolution does not lead to a nearby state, as in the case of a subcritical bifurcation, it is not necessary to impose specific disturbances to the flow in order to observe an instability. This is in part the reason that bifurcation points can be accurately determined in closed flow experiments: the instabilities are usually absolute.[38]

Convective instabilities, which can dominate in open flows,[39] are less straightforward to study. Since convective disturbances advect out of any finite length open system in finite time [Fig. 6(b)],[40] instability triggered by random noise can be detected only if the noise is amplified to detectable levels during the time of flight through the system. Thus, the more perfect (i.e., quieter) the laboratory flow facility, the more difficult it is to detect the onset of a convective
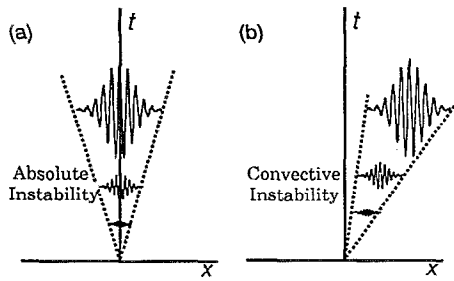
FIG. 6. Space-time diagrams illustrating the distinction between absolute and convective instability. (a) If an initially localized disturbance grows to fill all space, then the instability is absolute. (b) If the disturbance advects more quickly than it spreads, then the instability is convective.

instability.[3] Moreover, beyond the transition point where linear growth rates are sufficiently large to produce detectable signals within the time of flight through the system, there will generally be a band of unstable modes, and the flow dynamics can be quite irregular due only to the linear growth of a random mixture of uncorrelated modes.

In the absence of imposed disturbances, instability in our experiment is first marked by the appearance of a small broad peak in the power spectra for $R \approx 180$ (Fig. 7). The time variations in the velocity time series are indistinguishable from instrumental noise. If the background turbulence intensity is increased (by reducing the mechanical isolation of the channel; Sec. IV), the onset of waves is observed at smaller R. At larger R the time series displays oscillations whose frequency is relatively well defined, but whose phase and amplitude are quite variable. This behavior is reflected in power spectra that show a dominant peak with increased height and width. With $R > 200$, the oscillations become quite irregular, and spectra become broad and decrease nearly monotonically in power with increasing frequency (Fig. 7). Flow visualization reveals the presence of 2-D waves whose appearance, particularly for lower values of R above transition, is intermittent.

Direct evidence for a convective primary instability is provided by imposing pulsed flow rate disturbances (Sec. III B), and observing the subsequent evolution. Figure 8
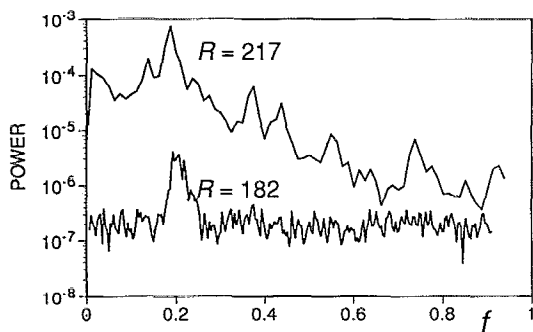

FIG. 7. Velocity power spectra at two values of R for the case of no imposed disturbances to the flow. The onset of unsteady flow is seen as broadband peaks. The measurements were obtained by laser Doppler velocimetry at x=117.1, y=0, and z=−5.1. The frequency and power spectral density are dimensionless.
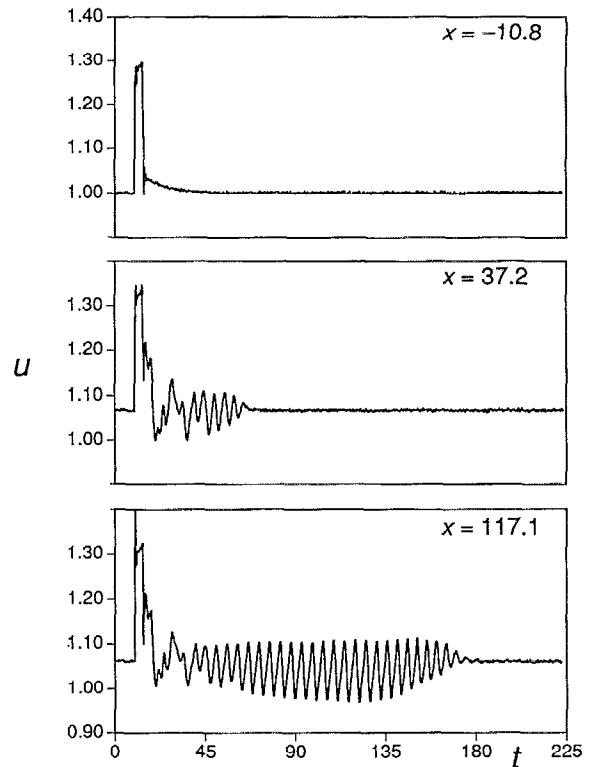

FIG. 8. Velocity time series measurements at R=165 showing the convective nature of the primary instability. Following a square flow-rate pulse (between times 10 and 14), the velocity decays rapidly to a steady state (parabolic profile) upstream of the cylinder array (x=−10.8). Within the periodic array of cylinders, the pulse disturbance excites a wave packet that advects downstream. The velocity initially evolves similarly at upstream (x=37.2) and downstream (x=117.1) locations separated by a distance 12L. The tail of the wave packet first advects past the upstream location, then past the downstream location. For all three time series, y=0 and z=−5.2.

shows time series at three locations in the experiment. Upstream of the cylinder array (x=−10.8 in Fig. 8), the velocity $u(y=0)$ quickly returns monotonically to U_{cl} after the end of the pulse. This time series demonstrates that the Poiseuille flow in the channel entrance is absolutely stable[37,41] at these Reynolds numbers; the time scale for the return to the parabolic profile is ~0.11R (approximately equal to 18 in Fig. 8), as obtained directly from the development length for Poiseuille flow.[21] By contrast, within the cylinder array (x=37.2 and 117.1 in Fig. 8), velocity time series evolve rapidly to oscillatory behavior; moreover, velocities at points with the same (y,z) and separated along x by an integer multiple of L (as in Fig. 8) initially evolve nearly identically because the flow pulse excites an L periodic wave packet within the cylinder array. The nonzero group velocity of the wave packet can be seen by comparing the time series at the upstream and downstream points: the oscillations quickly decay upstream but continue to evolve downstream. Eventually, the wave packet advects out of the experiment and the velocity everywhere becomes steady.

Flow visualization of impulsive disturbances in Fig. 9 provides another view of the convective instability. A pulse in the flow rate at t=0 excites a 2-D disturbance with several modes present. This disturbance quickly evolves into

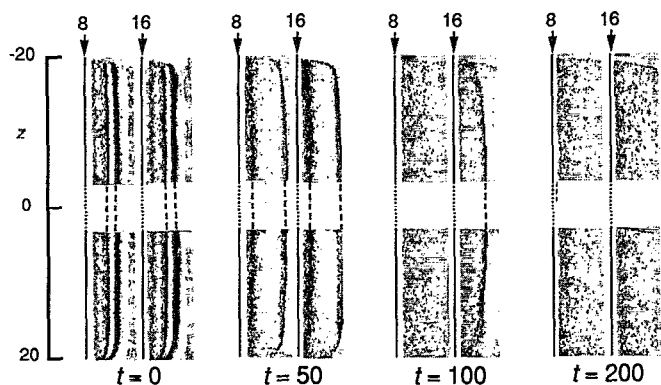Phys. Fluids, Vol. 7, No. 2, February 1995

Schatz, Barkley, and Swinney   349

FIG. 9. Dye visualizations illustrating the convective instability at $R=138$. Dye fronts at upstream (after cylinder 8) and downstream (after cylinder 16) locations are shown at four different times following a flow rate pulse ending at $t=0$ (cf. Fig. 8, $t=14$). The fronts are produced electrochemically at the cylinders, whose locations are indicated by thin vertical lines and numbered arrows. Near $z=0$, channel wall braces block a direct view of the flow; dashed lines are drawn to guide the eye. The two-dimensional disturbance quickly evolves into a traveling wave packet with wavelength $L/2$, as seen by $t=50$. The wave packet has advected out of the upstream region by $t=100$, but can still be seen in the downstream region. By $t=200$ the wave packet has advected out of the experiment. Dye is produced at cylinders 8 and 16 only; in the absence of any imposed disturbances, dye streams in continuous sheets from the dye-producing cylinders.

a 2-D traveling wave of wavelength $L/2$ (wave number $k=1.9$), as is seen by the presence of two dye fronts per cylinder spacing at $t=50$ in Fig. 9. This flow wavelength of one-half the geometric period L is in agreement with numerical simulations and previous experiments.[18,19] (Note, however, that the flow deviates slightly from a strict traveling wave because the cylinders break translational symmetry in the streamwise direction.) At $t=100$, the packet can be seen only in the downstream regions of the experiment. Finally, by $t=200$ the wave packet has advected out of the experiment.

Transition in numerical simulations is also strongly affected by the presence of convective instability, where boundary conditions play an essential role. With streamwise periodic boundary conditions, a disturbance that advects out of the downstream end is fed back in at the upstream end, and convective instability cannot be distinguished from absolute instability; after the onset of instability, a time series from a fixed spatial point shows limit cycle behavior that continues without interruption.[19] If, however, inflow–outflow streamwise boundary conditions are imposed, then the convective nature of the instability can be observed:[42] time series from fixed spatial points then show limit cycle behavior only for a finite time period, as in the experimental time series of Fig. 8.

B. Onset of instability: Supercritical bifurcation

A transition is *supercritical* (continuous) if the exponential growth of linear modes is ultimately saturated by nonlinearity at lowest order.[43] The secondary flow arising from a supercritical primary instability typically has a simple ordered structure resulting from the competition between a small number of modes. On the other hand, if nonlinearity is
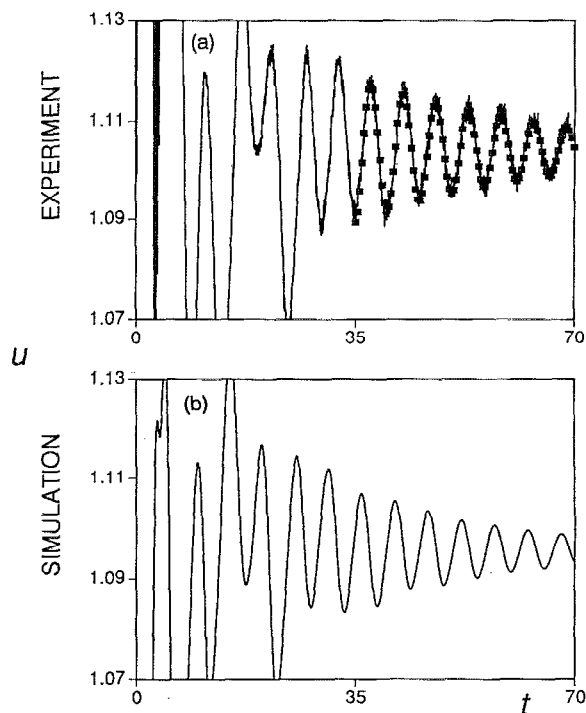

FIG. 10. Velocity time series at $R=110.5$ showing the decay of pulse disturbances below the onset of the primary instability in (a) experiment and (b) simulation. The points (■) in (a) correspond to a fit of the data to (14). The time series in both experiment and simulation are taken at the same location relative to the cylinder array ($x=3.9$ from the nearest upstream cylinder; $y=0$); in the experiment, $z=-5.1$.

destabilizing at lowest order, then the transition is *subcritical*: there is a discontinuous hysteretic jump to a finite-amplitude state, and for a range of R ($R<R_1$) the finite-amplitude state is bistable with the steady laminar state. Many modes can compete during the formation of the secondary flow, increasing the possibility of disorder. For example, in plane channel flow the primary instability is strongly subcritical[1,2] and the onset of turbulence can occur, even for R five times smaller than the critical value R_1.

The simple traveling wave nature of the secondary flow arising from the convective instability (Figs. 8 and 9) suggests that the primary instability is a supercritical Hopf bifurcation; our results show that this is indeed the case. (Note that a pitchfork bifurcation is not allowed, because continuous translational symmetry is broken in the periodic geometry; there is no comoving frame of reference in which the waves are steady.) For the present, we ignore spatial effects due to convective instability and focus on the dynamics at the center of evolved wave packets, where spatial variation is small.

The behavior in the vicinity of a Hopf bifurcation is captured by the Hopf normal form,[43]

$$\frac{dA}{dt}=(\sigma+i\omega)A-g|A|^2A, \tag{11}$$

where A is a complex amplitude, g is a positive real constant in the case of a supercritical bifurcation, σ is the growth rate, and ω is the frequency. With $A=\mathcal{A}e^{i\varphi}$, Eq. (11) becomes
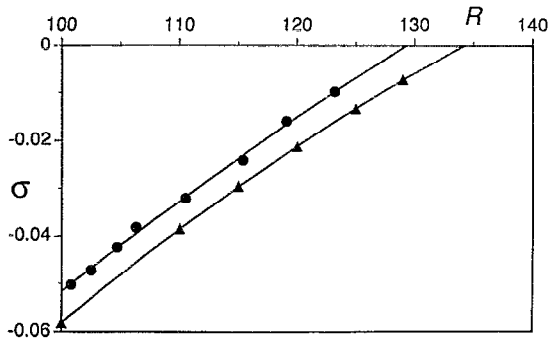
FIG. 11. The onset of the primary instability R_1 is determined from a plot of growth rate σ vs R; $R_1 = 129.3$ from the experiment (●) and $R_1 = 134.0$ from the linear stability analysis (▲). The solid lines are quadratic fits.

$$\frac{d\mathcal{A}}{dt} = \mathcal{A}(\sigma - g\mathcal{A}^2), \quad \frac{d\varphi}{dt} = \omega. \quad (12)$$

Here $\mathrm{Re}\{A\}$ can correspond to the time periodic part of any velocity component at some spatial location, and close enough to the bifurcation point, σ will be proportional to the parameter distance from the onset, i.e., $\sigma \sim \epsilon$, where $\epsilon \equiv (R - R_1)/R_1$.

Below transition all disturbances decay, and the equation for the modulus $\mathcal{A}$ becomes (for $\mathcal{A}$ sufficiently small)

$$\frac{d\mathcal{A}}{dt} = \mathcal{A}\sigma. \quad (13)$$

Hence, in the final stages of decay, $\mathrm{Re}\{A\}$ will be an exponentially decreasing sinusoid. This behavior is observed in the experimental and numerical velocity time series for $R < R_1$, as Fig. 10 illustrates. Note that equivalent spatial points in the measured and simulated velocities evolve nearly identically and differ in the mean by only 1%.

We obtain σ at each R in the experiment by fitting the exponentially decaying oscillations in the measured velocity time series to

$$u = b + A_0 \exp(\sigma t)\cos(\omega t + \gamma), \quad (14)$$

with b, A_0, σ, ω, and γ as free parameters; (14) fits the data well, as Fig. 10(a) illustrates.

Figure 11 shows plots of $\sigma(R)$ from both experiment and the linear stability computations. The critical value R_1 for the onset of the primary instability is obtained by extrapolating σ to zero growth rate. The range of R shown in Fig. 11 is sufficiently large that there is deviation from linear dependence on the parameter R (the relation $\sigma \sim \epsilon$ is expected to hold only for small ϵ); hence, $\sigma(R)$ is fit to a quadratic. We estimate $R_1 = 129.3 \pm 6.0$ for the experimental data, where the uncertainty includes an estimate of systematic as well as statistical errors. From the linear stability calculation we obtain $R_1 = 134.0$, which is 3.6% larger than the experimentally determined value.

For $R > R_1$ the oscillations no longer decay exponentially, but, as seen in Fig. 12(a), they grow until saturated by nonlinearity (before the tail of the wave packet advects past the probe in the experiment). From the Hopf normal form, A_0 has a stable asymptotic value at saturation given by A_0
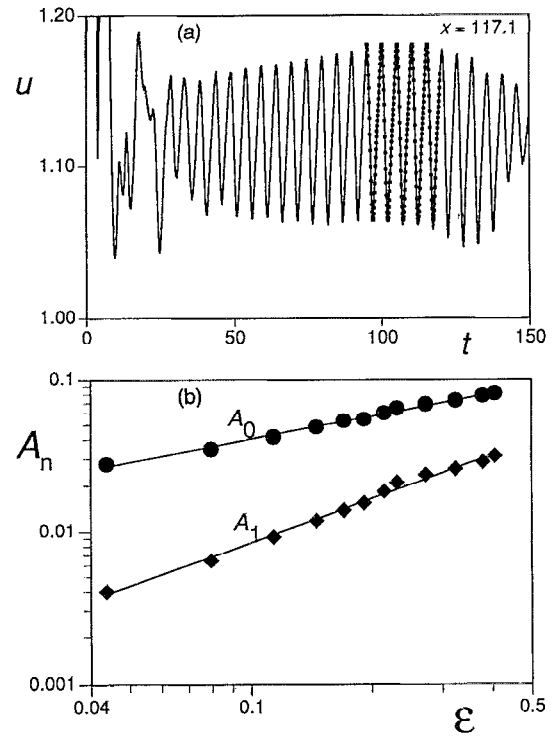

FIG. 12. Experimental evidence for a supercritical primary transition. (a) Growth and saturation of disturbances above the onset of the primary instability is illustrated by a velocity time series at $R = 151.2$ ($y = 0$, $z = -5.1$). A least-squares fit to (15) is also shown (■). The decay of the time series near $t = 150$ is due to the advection of the wave packet past the point of observation. (b) Saturation amplitudes A_0 (●) and A_1 (♦) vs $\epsilon \equiv (R - R_1)/R_1$.

$= \sqrt{\sigma/g} \sim \sqrt{\epsilon}$. Higher-order nonlinearity is also responsible for harmonic generation not contained in the normal form. The harmonics A_n scale as $\epsilon^{(n+1)/2}$ for $n = 1,2,3,\ldots$. To investigate for $R > R_1$, we fit saturated regions of the velocity time series to

$$u = b + A_0 \cos(\omega t + \gamma_0) + A_1 \cos(2\omega t + \gamma_1), \quad (15)$$

with b, A_0, A_1, ω, γ_0, and γ_1 as free parameters. With $R_1 = 129.3$ for the experiment, linear regression fits of A_0 and A_1 vs ϵ yield exponent estimates of 0.50 ± 0.01 for A_0 and 0.95 ± 0.02 for A_1 in the experiment [see Fig. 12(b)].

The time-asymptotic amplitude (i.e., the amplitude sufficiently far downstream) is independent of the form of imposed disturbances. Figure 13 shows that downstream the amplitudes measured for flows triggered by impulsive disturbances agree within 5%–10% with the amplitudes measured for flows triggered by 2-D time-periodic disturbances, even though the upstream amplitudes can differ considerably for different disturbances. The frequencies of the time-periodic disturbances are fixed to within 5% of the natural frequencies selected by impulsive disturbances; measurements made for a range of disturbance frequencies reveal a resonance response peaked near the frequency selected by impulsive disturbances. For fixed R, the initial time-periodic disturbance amplitude can be varied by altering the angular foil amplitude ϕ: as ϕ increases, A_0 measured upstream increases in

Phys. Fluids, Vol. 7, No. 2, February 1995
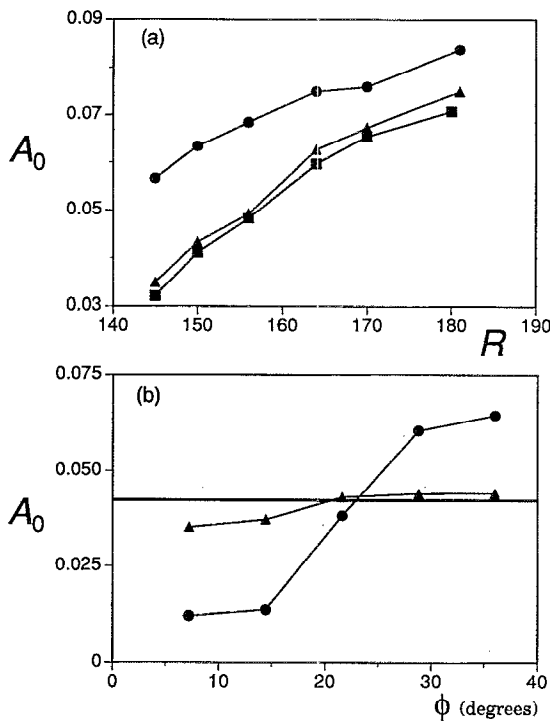
Schatz, Barkley, and Swinney   351

FIG. 13. Plots showing the insensitivity of the downstream saturation amplitude of the secondary flow to the form of imposed disturbances. (a) Downstream (x=117.1) amplitude of fundamental A_0 as a function of R, both for impulsive disturbances (■) and for two-dimensional time-periodic disturbances with ϕ=36° (▲). Also shown for time-periodic disturbances is the upstream amplitude [at x=37.2, 12L upstream of x=117.1(●)]. (b) Amplitude A_0 as a function of the disturbance foil displacement ϕ at R=150 for time-periodic disturbances [x=37.2(●) and x=117.1(▲)]. The solid horizontal line indicates A_0 from impulsive disturbances. In both (a) and (b), y=0, z=−5.2, and A_0 represents the root-mean-square (RMS) amplitude of the fundamental.
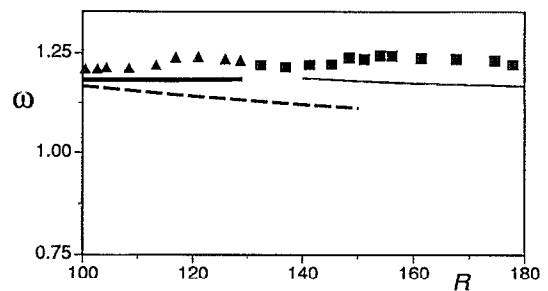

FIG. 14. Comparison of frequencies in the spatially periodic channel flow and in plane channel (Poiseuille) flow. Experimentally measured frequencies before (▲) and after (■) the primary transition; numerical linear eigenfrequencies for spatially periodic channel flow before transition (thick solid line); traveling wave frequencies from simulations after transition (thin solid line); and linear eigenfrequencies for plane Poiseuille flow (dashed line).[59] The flow in the plane channel is globally stable in this Reynolds number range.

value from less than to greater than A_0 for impulsive disturbances, as Fig. 13(b) illustrates, while the downstream amplitude converges to the same value as for the impulsive disturbances.

The secondary flow in the spatially perturbed channel has characteristic frequencies very similar to those for plane channel flow.[10] Figure 14 demonstrates that the frequencies of the traveling waves in the spatially perturbed flow lie within approximately 10% of the least stable linear modes (Tollmien–Schlichting waves) in plane Poiseuille flow, and also the traveling waves share a similar weak dependence of frequency on R.

While cylinders are used to provide spatial periodicity in the channel, the flow is very different from unbounded flow past a cylinder. In the latter case, the frequency of vortex shedding depends strongly on R near the onset,[44] and the oscillations are self-sustaining, because the transition arises from an absolute rather than convective instability.[37,45,46] Although spatially periodic channels exhibit strongly inflectional velocity profiles near the geometric perturbations, such profiles rapidly relax to a more nearly parabolic shape, yielding a mean vorticity field similar to that present in channel flow.[10] As a consequence, flow structures display the character of channel modes rather than cylinder wake modes. Karniadakis et al.[10] found numerical evidence that suggests cyl-

inder wake modes may be important if the channel flow is not fully developed.

C. One-dimensional (1-D) model system

We now present a one-dimensional (1-D) model that illustrates very simply the dynamics that results from a supercritical convective instability. One-dimensional models, most notably the Ginzburg–Landau equation, have been widely used to illustrate and understand essential features of convective instabilities.[9,46,47] However, the Ginzburg–Landau model is not well suited for our purposes, since the unstable mode at onset has a zero wave number. For modeling the primary instability in the channel, we require the following: (1) the primary bifurcation must be supercritical (i.e., nonlinear terms should saturate the instability); (2) the instability must be strongly convective (i.e., the group velocity should not only be nonzero at onset, but also remain convectively unstable far above onset); (3) the equations must be periodic in space to model the periodic channel geometry; and (4) the bifurcating wave number must be nonzero. A simple model having all of these characteristics is the convective Swift–Hohenberg equation, that is, the Swift–Hohenberg model with a first-derivative advective term:

$$\partial_t \Psi = \epsilon(x)\Psi - \Psi^3 - c\ \partial_x \Psi - (\partial_x^2 + 1)^2 \Psi, \tag{16}$$

where Ψ is a real amplitude and ϵ and c are parameters with ϵ a periodic function of x.

If ϵ is independent of x, the homogeneous state (Ψ=0) becomes unstable in a supercritical bifurcation at ϵ=0. The critical wave number of the instability is k=1 and the group velocity at onset is c. Hence, by choosing c large (~10), the primary instability will be strongly convective. We make $\epsilon(x)$ periodic with wave number $k=\frac{1}{2}$, so that the spatial periodicity of the equation will be twice that of the waves at onset. [Recall that the spatial period of the channel is twice the period of the waves arising at the primary instability (Fig. 9).] To model an open system, we impose the boundary conditions $\partial_x \Psi = \partial_{xxx}\Psi$=0 at both ends of an interval [0,100]. The general phenomena do not depend sensitively on the
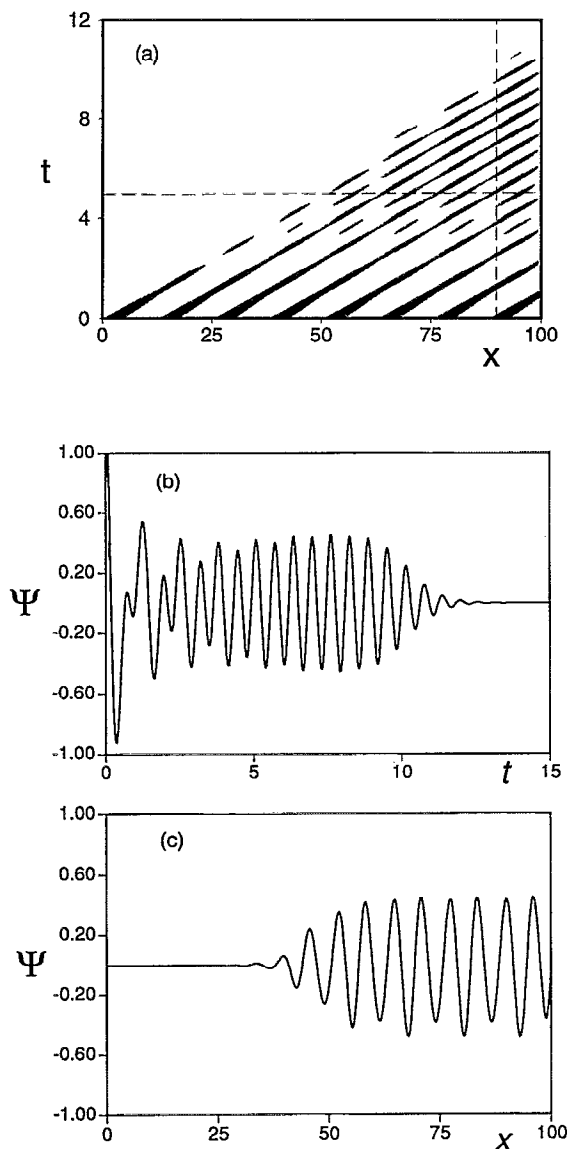
FIG. 15. (a) Space-time diagram illustrating supercritical transition arising from convective instability in a model, Eq. (16). Points where $\psi > 0.34$ are shown as black. Parameter values are given in the text. The solution is initially dominated by wave number $k = \frac{1}{2}$ [the wave number of the "geometry" $\epsilon(x)$]. As the wave propagates out of the system, the solution evolves to a state with wave number $k = 1$ (the unstable wave number of the system). (b) Time series at $x = 90$ [indicated by a vertical dashed line in (a)]. (c) Spatial profile $t = 5$ [indicated by a horizontal dashed line in (a)].

type of boundary conditions used; however, for reasons mentioned earlier, the boundary conditions must not be periodic.

Figure 15 shows the results of numerical simulations of (16) for $c = 10$ and $\epsilon(x) = 0.25 + \sin(x/2)$. There is a transition to a well-ordered saturated state that advects through the system. Figure 15(a) shows a space–time plot and Figs. 15(b) and 15(c) show, respectively, a time series at a fixed spatial location and a spatial profile at a fixed time. The space-time plot in Fig. 15(a) is strikingly similar to that obtained by full numerical simulations of the Navier–Stokes equations for flow in the periodic channel geometry.[42] Initially, the solution has a wave number $k = \frac{1}{2}$, but evolves to a state dominated by the $k = 1$ mode. The time series in Fig. 15(b) is quite

similar to the experiment time series in Fig. 12: the amplitude saturates briefly and is followed by a decay as the state advects past the spatial point.

VI. SECONDARY INSTABILITY

In many open flows, secondary instability marks the beginning of a rapid progression to turbulence.[24,48–50] In spatially periodic channel flow, however, the 2-D traveling waves undergo a secondary instability to a well-ordered, stable, 3-D flow with an additional periodicity in the streamwise direction that is different from that of the secondary flow.[51] In this section we describe the tertiary state and present data for the onset of the secondary instability and for the selection of spanwise wave number of the subsequent flow.

A. Qualitative description: Standing waves

The secondary instability, like the primary instability, is convective, which presents difficulties in observing it in a finite length system. The secondary instability is even more difficult to observe than the primary instability, because small-amplitude fluctuations grow initially only via the primary instability mechanism; the secondary instability mechanism comes into play only after the secondary flow reaches sufficient amplitude. In our experiment without imposed disturbances, 3-D flow is observed only for R well above 200 after a strong 2-D flow is established. The 3-D behavior appears irregularly along the span and is stronger near the span walls, where 3-D disturbances are larger.

We must impose 3-D disturbances if the secondary instability is to develop sufficiently to be observed during the time of flight through our experiment. (The 3-D time-periodic disturbances imposed in our experiments are described in Sec. III.) Beyond the bifurcation point for the secondary instability, the traveling waves develop nearly sinusoidal variations in the spanwise direction z with a standing wave behavior in the *streamwise* direction, as Fig. 16 illustrates. That is, at a fixed time, the spanwise phase of the wave downstream is shifted by 180° relative to the wave located upstream. Compare, for example, the dye front between cylinders 13 and 14 with that between cylinders 8 and 9 in Figs. 16(a) and 16(b). Dye fronts from intermediate cylinders show the standing wave at other phases. Dye fronts become nearly 2-D between cylinders 10 and 11 in Fig. 16(a). The front does not become completely flat, because cylinders are not necessarily located at the nodal lines of the standing wave and because the dye fronts are indicators of the streaklines rather than streamlines in the flow. Farther downstream (not shown in Fig. 16), another 180° phase change can be observed in a dye front just before the channel exit. The streamwise wave number of the tertiary flow at onset is 0.09 ± 0.02 and increases with increasing R.[52]

The standing wave pattern does not drift downstream: for fixed experimental conditions, the phase of the standing wave is locked in the lab frame. Evidence for this can be found in power spectra from a probe fixed in the laboratory frame—the spectra show only one fundamental frequency, that of the imposed disturbance. These spectra are qualitatively indistinguishable from those of 2-D time periodic dis-
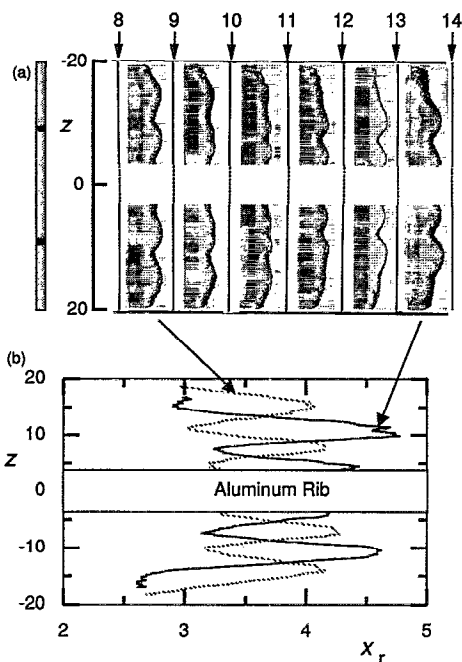
FIG. 16. One-half cycle of the three-dimensional standing wave state at $R=170$ arising from secondary instability. (a) The standing wave pattern is visualized with dye produced electrochemically at the nearest upstream cylinder for each wave front. Cylinder locations are indicated by thin vertical lines and numbered arrows. Each dye front is recorded separately in time, but the temporal periodicity of the flow allows all dye fronts to be combined in this composite image. Near $z=0$, channel wall braces block a direct view of the flow; dotted lines are drawn to guide the eye. (b) Streamwise local maxima of the standing wave dye fronts are shown upstream (dashed line) and downstream (solid line) by plotting the distance from the nearest upstream cylinder x_r as a function of z. In both (a) and (b) initial three-dimensionality is imposed on the flow by two protuberances on the disturbance foil, illustrated at the far left in (a). The center-to-center spacing of the protuberances imposes an initial wave number $k_z^0=0.42$; the flow selects $k_z=0.9$.
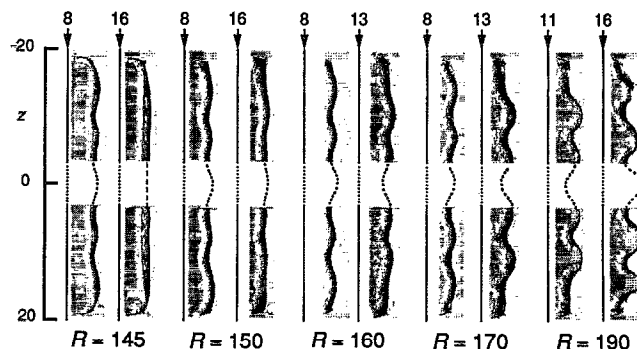

FIG. 17. Onset of secondary instability illustrated by dye visualization. Local standing wave maxima are shown simultaneously at upstream and downstream regions of the experiment for several Reynolds numbers. The imposed disturbance decays (grows) as it advects downstream for $R<160$ ($R>160$). As in Fig. 16, k_z^0 is 0.42.

A quantitative determination of R_2 is made by analyzing digitized dye fronts. The location of the dye fronts is determined by thresholding the image intensity and averaging along the streamwise direction. The amplitude of each dye front is characterized by the RMS value of its streamwise position. Care is taken to compare dye fronts with similar mean streamwise positions relative to the upstream dye-producing cylinder; a typical result is shown in Fig. 16(b). This analysis yields the ratio of downstream to upstream amplitudes of the 3-D component in the flow. Figure 18(a) shows this amplitude ratio as a function of R. Taking the point where the amplitude ratio crosses 1 to be the onset of
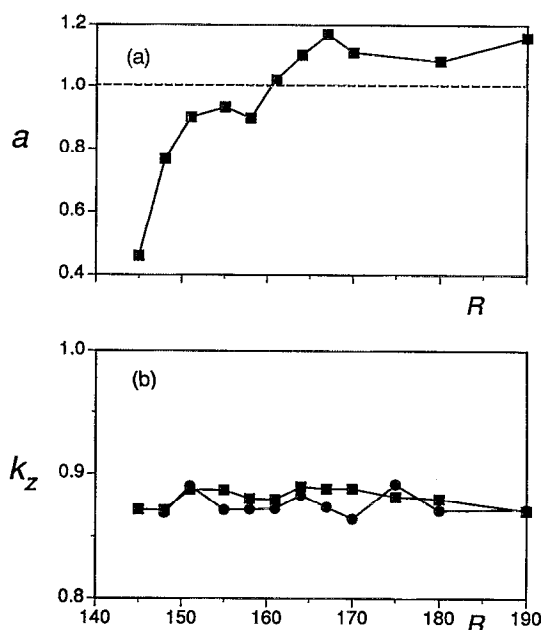
turbances; however, in any other reference frame, the standing wave would lead to an additional spectral component. We speculate that the phase of the standing wave is locked because our method of imposing disturbances fixes the phase at the inlet (see Sec. VI C).

B. Onset of secondary instability

We have determined the critical Reynolds number R_2 for the onset of the secondary instability by finding the crossover from downstream decay to downstream growth of imposed 3-D disturbances. To distinguish growth from decay, the amplitude of the wave is compared at successive streamwise maxima. For example, compare the dye front between cylinders 8 and 9 to the dye front between cylinders 13 and 14 in Fig. 16(b). A rough estimate for R_2 can be obtained by comparing upstream–downstream dye front pairs for several values of R (see Fig. 17). For sufficiently small R (e.g., $R=145$ in Fig. 17), the sinusoidal variation along z that is present upstream does not appear downstream; thus, 3-D disturbances decay. For larger R, however, the downstream dye fronts are more distorted than the upstream fronts (e.g., $R=190$ in Fig. 17), indicating that the 2-D traveling wave is now 3-D unstable.

FIG. 18. (a) Ratio a of the downstream to upstream standing wave amplitude as a function of R. For $R<160$, $a<1$ (amplitude decays downstream), while for $R>160$, $a>1$ (amplitude grows downstream). (b) Spanwise wave numbers k_z as a function of R for upstream (■) and downstream (●) locations. In both (a) and (b) k_z^0 is 0.42, and each data point represents the average for seven digitized dye fronts like those shown in Fig. 16(b).
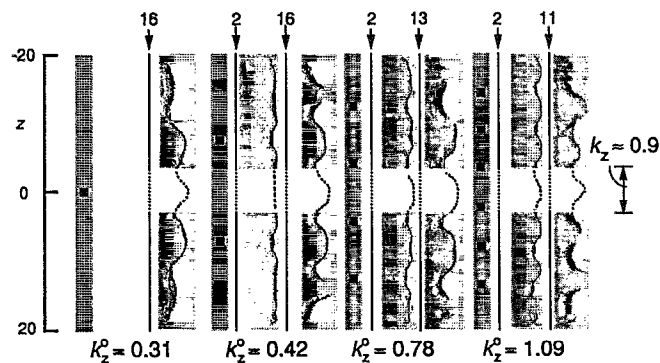
FIG. 19. Images showing the selection of the spanwise wave number $k_z=0.9$ at $R=190$. Upstream flow disturbances are caused by the foil with protuberances at z locations indicated (■). The initial form of the flow disturbances is seen by dye visualizations at cylinder 2 for $R=160$. The wave numbers of the initial disturbances are given below the dye front images. (No image for cylinder 2 with $k_z^0=0.31$ is available.)

FIG. 21. Growth rate of the secondary instability as a function of the spanwise wave number determined from a Floquet analysis for the geometry shown in Fig. 1 for $R=150$ (●) and $R=160$ (▲). Interpolation gives values for the onset of the secondary instability: $R_2=152$ and $k_z=0.8$.

the secondary instability, we obtain $R_2=160\pm5$, which is well separated in Reynolds number from the primary instability at $R_1=129.3$.

The onset of secondary instability is found to occur at $R_2\approx160$, independent of selected variations in the imposed 3-D disturbance:[52] changes in the foil oscillation frequency by $\pm5\%$, in the foil amplitude ϕ between 25° and 50° (Fig. 5), and in the protuberance length l_b between 0.88 and 3.5 (Fig. 5 and Table I).

C. Selection of spanwise wave number

The spanwise wave number k_z of the secondary flow is measured by fitting the peaks and valleys of the dye front images to parabolas and then computing the distance between these extrema. Figure 18(b) shows that k_z is essentially independent of the streamwise location and of R over the range investigated.

Figures 19 and 20 illustrate the selection of $k_z\approx0.9$ for a range of different imposed spanwise wave numbers k_z^0 (see Fig. 5 and Table I). The initial form of 3-D disturbances introduced to the flow can be seen in the upstream dye visualization of Figs. 19 and 20. With protuberances well separated along z, the dye fronts are 2-D, except for small "val-
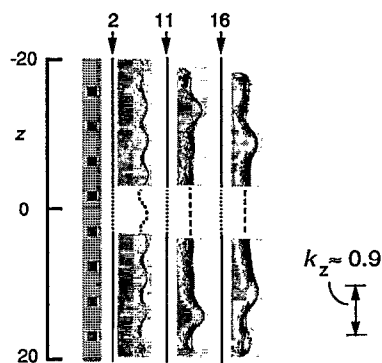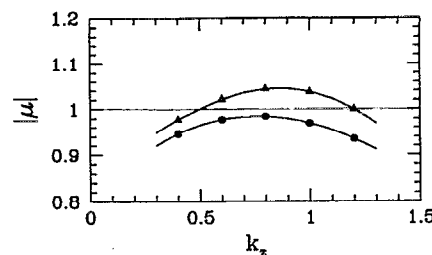

FIG. 20. Selection of wave number $k_z\approx0.9$ for an initial disturbance with a wave number of 1.40 ($R=190$).

leys" located at the same z position as the protuberances; with an increasing number of protuberances, the valleys move closer together, and the dye front appears nearly sinusoidal. This inlet behavior sets the initial condition on the phase of the standing wave that evolves downstream.

Downstream for $k_z^0\approx0.9$, the standing wave is observed to maintain $k_z\approx k_z^0$ ($k_z^0=0.78$ and $k_z^0=1.09$ in Fig. 19). With k_z^0 significantly smaller, the standing wave evolves directly to $k_z^0\approx0.9$ ($k_z^0=0.31$ in Fig. 19—also see Figs. 16 and 17 for which $k_z^0=0.42$). In the case of $k_z^0=0.31$, counterpropagating waves evolve from a localized three-dimensionality at $z=0$ on the disturbance foil; as the flow progresses from upstream to downstream, these waves propagate to the span walls and form the state that is observed in Fig. 19. For k_z^0 significantly larger than 0.9, counterpropagating waves of $k_z\approx0.9$ are observed, but the waves are just beginning to propagate from the span walls toward the center (Fig. 20); the waves are expected to develop fully into standing waves sufficiently far downstream, although the present channel is too short to confirm this conjecture. All runs satisfied $l_b/l_g<1$. For $l_b/l_g>1$, the effect of the imposed disturbance persisted throughout the streamwise length of the channel, but we believe that even in this case a preferred wave number would be selected in a longer channel.

D. Comparison with Floquet stability analysis

Using the numerical Floquet stability analysis described in Sec. IV, we examine the 3-D stability of the 2-D traveling wave state. The 2-D traveling wave base flows at $R=150$ and $R=160$ are obtained by direct simulations. The most detailed stability analysis is performed for Floquet modes in the $n=1$ computational domain (i.e., for a single period of the periodic array of cylinders).[53] Figure 21 shows the magnitude of Floquet multipliers versus k_z; a linear interpolation between the maximum of each curve yields $R_2=152$ (where $|\mu|$ goes through 1) for a mode with wave number $k_z=0.8$. The Floquet multiplier is complex at the bifurcation point, and is given by $\mu_c=0.964\pm0.267i$.

We also investigate how the spectrum of multipliers depends on the streamwise periodicity of the Floquet mode. For these computations, we fix $R=150$ and $k_z=0.8$, and vary the streamwise periodicity of the Floquet modes by computing in domains of period nL, $n>1$. We classify the modes according to the domain size n; the leading multipliers for

TABLE II. Floquet multipliers for $R=150$ and $k_z=0.8$ from linear stability analysis for secondary instability. Between the two period-1 eigenvalues shown, there are no other period-2 modes; however, there may be additional period-3 and period-4 modes.

Spatial period	$\text{Re}(\mu)$	$\text{Im}(\mu)$	$|\mu|$
1	0.949 139	0.277 078	0.9888
4	0.170 527	0.967 495	0.9824
4	0.651 889	0.728 031	0.9773
3	0.351 565	0.910 218	0.9758
2	−0.2908	0.921 402	0.966
3	−0.192 885	0.936 128	0.9558
3	−0.738 626	0.562 692	0.9285
4	−0.843 916	0.316 609	0.9014
1	−0.718 767	0.327 159	0.809

FIG. 22. Velocity power spectra from simultaneous upstream ($x=36.9$) and downstream ($x=117.1$) measurements for R far above the onset of the secondary instability: $R=207$. Upstream the flow is periodic while downstream the spectrum contains a broad subharmonic peak. Both spectra were recorded at $y=0$ and $z=-5.2$. 3-D time-periodic disturbances with $k_x^0=0.9$ have been imposed.

$n<5$ are listed in Table II. Although the single $n=1$ mode has the multiplier of largest magnitude, the multipliers are very closely spaced in magnitude. We have attempted to compute the stability of modes with $n=10$, but without success. Our method for computing multipliers depends upon gaps in the multiplier spectrum; apparently, for large n the spectral gaps are too small (the multipliers are too closely spaced) for us to achieve convergence with a reasonable computation time (i.e., within 100 iterations of the operator A defined in Sec. IV).

The computed value of $R_2=152$ is in reasonable agreement with the experimentally determined value of $R_2=160\pm5$, and the computed critical wave number 0.8 agrees with the measured value, 0.9 ± 0.2. Experiment suggests that the instability corresponds to a mode with $n\approx10$. Since the multipliers obtained from the computations for smaller values of n are closely spaced (for fixed R and k_z), and since the spatial Floquet exponents are small for n large (the spatial exponent is zero for $n=1$),[50] the bifurcation point for the dominant $n=10$ mode should be at approximately the same point as for the $n=1$ mode. Nevertheless, we cannot explain why an $n\approx10$ mode is dominant in the experiment. This could be due to nonlinearity or to the method of imposing disturbances. Finally, we note that all multipliers we computed for the secondary instability are complex. In particular, the critical mode for $n=1$ is complex, and this corresponds to a bifurcation to a nonzero secondary frequency in the laboratory frame. Such a secondary frequency is not observed in experiment, perhaps due to the phase locking of the standing wave as discussed in Sec. VI A.

E. Beyond secondary instability

We have not investigated in detail flows well beyond R_2, but we note that the appearance of broadband subharmonics in the power spectra indicates another transition in the flow. For $R>190$, the power spectra of data acquired near the inlet show only the fundamental and harmonics [Fig. 22(a)], while downstream [Fig. 22(b)], a broad subharmonic peak appears. The appearance of this peak only in downstream spectra suggests that the additional frequencies are not the result of subharmonics being advected from the disturbance foil at the
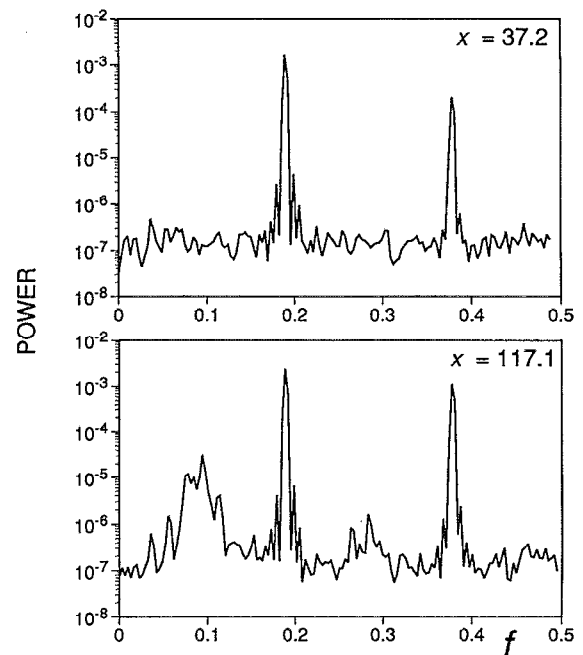
inflow. These spectra are reminiscent of broad subharmonic peaks seen in other transitional wall-bounded shear flows.[54]

VII. DISCUSSION AND CONCLUSIONS

Instability of the steady laminar state in spatially periodic channel flow does not necessarily lead to a disordered, high-dimensional, turbulent state,[10,18,20] as is typically the case in open flows. Our laboratory experiments and numerical computations demonstrate the existence of stable flow states with low-dimensional dynamics arising from primary and secondary transitions in a spatially periodic channel flow. 2-D waves are stable for a range of R above the primary transition at $R_1=130$, and stable three-dimensional waves arise from secondary instability at $R_2\approx160$. The experimental and linear stability results are in good agreement for the onset of both transitions, the frequency ($\omega=1.2$) and streamwise wave number ($4\pi/L=1.9$) of the secondary flow, and the spanwise wave number (0.9) of the tertiary flow.

In our laboratory experiments, we visualize and characterize 2-D and 3-D wave states that are observed only fleetingly in typical wall-bounded shear flows.[3] The supercritical primary instability in the spatially periodic channel leads to stable 2-D *channel* modes similar to the Tollmien–Schlichting modes of plane channel flow[10] (and different from modes associated with bluff body vortex shedding).[44] The 3-D tertiary flow observed experimentally with streamwise wave number (0.1) is a "detuned" mode (the streamwise period is neither the same as nor a subharmonic of the 2-D secondary flow), similar to those found in other

Schatz, Barkley, and Swinney

wall-bounded shear flows.[50] The observed 3-D waves remain stable as they propagate down the channel, in contrast to waves in plane channels and boundary layers, which are observable for a few wavelengths (if at all) before the flow becomes turbulent.[49,55] Our Floquet stability analysis shows that the most unstable mode is a "fundamental" (both the secondary and the tertiary flows have the same streamwise period); however, detuned modes of increasing wavelength are nearly equally unstable, so at linear order there is not a strong selection for any particular streamwise mode. A small second frequency (0.008) from stability analysis is not observed in the experiment.

Convective instability plays a crucial role in the periodic channel flow. Transition triggered solely by background disturbances yields a misleading picture of onset. The intermittent transition and variation in transport properties observed over a broad range of R in earlier experiments[13,17] can be understood as arising from the convectively unstable amplification of uncontrolled (ambient) disturbances. Controlled disturbances with different spatial and temporal properties help elucidate both linear and nonlinear aspects of transition, but as we have emphasized, it is also important to verify that asymptotic behavior is independent of the properties of the disturbances. Our results suggest a way convective instability may be used to advantage in engineering flows employing unsteady laminar transport: just above the onset of unsteadiness, the approach to asymptotic conditions occurs more rapidly when well-chosen time-periodic disturbances are introduced *locally* upstream. Our simple 1-D model successfully mimics the essential features of the primary transition and demonstrates that convective instability in an open flow need not evolve spatially to turbulence, as might be inferred from other 1-D model results.[56,57]

Our results, in conjunction with previous simulations,[10] suggest that geometry can play the role of an additional "control parameter" in channel flow. Variations of this parameter can unfold the bifurcations, leading to different flow states. For example, the spatially periodic channel considered here is conceptually obtained from plane channel flow by setting the "geometrical parameter" to some nonzero value; as a consequence, the primary transition changes from sub- to supercritical. Hence, there must exist some intermediate value where the bifurcation is degenerate, i.e., crosses over from subcritical to supercritical. Under certain circumstances, this situation may permit chaotic dynamics arbitrarily close to the laminar state.[6]

The onset of turbulence in spatially periodic channel flow remains unexplored. The broad subharmonic peak we observe for $R > 190$ may signal the onset of chaos, as is the case for some closed flows.[58] For $R \gtrsim 300$, the power spectra are broadband with no sharp spectral components. Future studies should examine this flow to determine whether the flow undergoes a transition from convective to absolute instability, and whether the flow is low or high dimensional.

Future studies should further examine transport in the spatially perturbed geometry. Can concepts from nonlinear dynamics be exploited to obtain more efficient transport of heat or mass using channels with spatially periodic perturbations? Channels with spatially periodic forcing should serve as a test bed for applications, as well as for addressing fundamental questions about instabilities and transition in open flows.

[1]S. Orszag, "Accurate solution of the Orr–Sommerfeld stability equation," J. Fluid Mech. **50**, 689 (1971).

[2]D. R. Carlson, S. E. Widnall, and M. F. Peeters, "A flow-visualization study of transition in plane Poiseuille flow," J. Fluid Mech. **121**, 487 (1982).

[3]M. Nishioka, S. Iida, and Y. Ichikawa, "An experimental investigation of the stability of plane Poiseuille flow," J. Fluid Mech. **72**, 731 (1975).

[4]T. Herbert, "Periodic secondary motions in a plane channel," in *Lecture Notes in Physics*, edited by A. I. van de Vooren and P. J. Zandbergen (Springer-Verlag, Berlin, 1976), Vol. 59, p. 235.

[5]J. D. Pugh and P. G. Saffman, "Two-dimensional superharmonic stability of finite-amplitude waves in plane Poiseuille flow," J. Fluid Mech. **194**, 295 (1988).

[6]D. Barkley, "Theory and predictions for finite-amplitude waves in two-dimensional plane Poiseuille flow," Phys. Fluids A **2**, 955 (1990).

[7]I. Soibelman and D. I. Meiron, "Finite-amplitude bifurcations in plane Poiseuille flow: Two-dimensional Hopf bifurcation," J. Fluid Mech. **229**, 389 (1991).

[8]Since transition depends on several parameters, parameter combinations can exist where an abrupt hysteretic transition occurs in closed flows—see, for example, D. Coles, "Transition in circular Couette flow," J. Fluid Mech. **21**, 385 (1965).

[9]M. C. Cross and P. C. Hohenberg, "Pattern formation outside of equilibrium," Rev. Mod. Phys. **65**, 851 (1993).

[10]G. E. Karniadakis, B. B. Mikic, and A. T. Patera, "Minimum-dissipation transport enhancement by flow destabilization: Reynolds' analogy revisited," J. Fluid Mech. **192**, 365 (1988).

[11]Several recent experimental studies have focused on open flow transition in different contexts; see, for example, K. L. Babcock, G. Ahlers, and D. S. Cannell, "Noise-sustained structure in Taylor–Couette flow with through-flow," Phys. Rev. Lett. **67**, 3388 (1991); J. Liu, J. D. Paul, and J. P. Gollub, "Measurements of the primary instabilities of film flows," J. Fluid Mech. **250**, 69 (1993); A. Tsameret and V. Steinberg, "Noise-modulated propagating pattern in a convectively unstable system," Phys. Rev. Lett. **67**, 3392 (1991).

[12]M. S. Isaacson and A. A. Sonin, "Sherwood number and friction factor correlations for electrodialysis systems, with application to process optimization," Ind. Eng. Chem. Process Des. Dev. **15**, 313 (1976).

[13]K. D. Stephanoff, "Self-excited shear-layer oscillations in a multi-cavity channel with a steady mean flow," ASME J. Fluid Eng. **108**, 338 (1986).

[14]F. P. Incropera, "Convective heat transfer in electronic equipment cooling," ASME J. Heat Transfer **110**, 1097 (1988).

[15]H. Kozlu, B. B. Mikic, and A. T. Patera, "Minimum-dissipation heat removal by scale-matched flow destabilization," Int. J. Heat Mass Transfer **31**, 2023 (1988).

[16]T. Mullin and S. R. Martin, "Intermittent phenomena in the flow over a rib roughened surface," ASME J. Fluid Eng. **113**, 206 (1991).

[17]M. Greiner, R. F. Chen, and R. A. Wirtz, "Heat transfer augmentation through wall-shape-induced flow destabilization," ASME J. Heat Transfer **112**, 336 (1990).

[18]H. Kozlu, "Experimental investigation of optimal heat removal from a

Phys. Fluids, Vol. 7, No. 2, February 1995

Schatz, Barkley, and Swinney   357

surface," Ph.D. thesis, Massachusetts Institute of Technology, 1989.

[19]G. E. Karniadakis, "The spectral element method applied to heat transport enhancement by flow destabilization," Ph.D. thesis, Massachusetts Institute of Technology, 1987.

[20]C. H. Amon and A. T. Patera, "Numerical calculation of stable three-dimensional tertiary states in grooved-channel flow," Phys. Fluids A **1**, 2005 (1989).

[21]H. Schlichting, *Boundary Layer Theory*, 6th ed. (McGraw-Hill, New York, 1968).

[22]T. Morel, "Design of two-dimensional wind tunnel contractions," ASME J. Fluid Eng. **99**, 371 (1977).

[23]W. Merzkirch, *Flow Visualization*, 2nd ed. (Academic, Orlando, FL, 1987).

[24]P. S. Klebanoff, K. D. Tidstrom, and L. M. Sargent, "The three-dimensional nature of boundary-layer instability," J. Fluid Mech. **12**, 1 (1962).

[25]T. C. Corke and R. A. Mangano, "Resonant growth of three-dimensional modes in transitioning Blasius boundary layers," J. Fluid Mech. **209**, 93 (1989).

[26]Y. S. Kachanov, "Physical mechanisms of laminar-boundary-layer transition," Annu. Rev. Fluid Mech. **26**, 411 (1994).

[27]R. D. Henderson, "Unstructured spectral element methods; parallel algorithms and simulations," Ph.D. thesis, Princeton University, 1994.

[28]A. T. Patera, "A spectral element method for fluid dynamics; laminar flow in a channel expansion," J. Comput. Phys. **54**, 468 (1984).

[29]G. E. Karniadakis, E. T. Bullister, and A. T. Patera, "A spectral element method for solution of two- and three-dimensional time-dependent Navier–Stokes equations," in *Proceedings of the Europe–US Conference on Finite Element Methods for Nonlinear Problems* (Springer-Verlag, New York, 1985), p. 803.

[30]G. E. Karniadakis, "Spectral element simulations of laminar and turbulent flows in complex geometries," Appl. Num. Math. **6**, 85 (1989).

[31]G. E. Karniadakis and G. S. Triantafyllou, "Three-dimensional dynamics and transition to turbulence in the wake of bluff objects," J. Fluid Mech. **238**, 1 (1992).

[32]I. Goldhirsh, S. A. Orszag, and B. K. Maulik, "An efficient method for computing leading eigenvalues and eigenvectors of large asymmetric matrices," J. Sci. Comput. **2**, 33 (1987).

[33]P. S. Marcus and L. S. Tuckerman, "Numerical simulation of spherical Couette flow. Part I: Numerical methods and steady states," J. Fluid Mech. **185**, 1 (1987).

[34]C. Mamun and L. S. Tuckerman, "Asymmetry and Hopf bifurcation in spherical Couette flow," Phys. Fluids **7**, 80 (1995).

[35]W. S. Edwards, L. S. Tuckerman, R. A. Friesner, and D. Sorensen, "Krylov methods for the incompressible Navier–Stokes equations," J. Comput. Phys. **110**, 82 (1994).

[36]D. S. Watkins, "Some perspectives on the eigenvalue problem," SIAM Rev. **35**, 430 (1993).

[37]P. Huerre and P. A. Monkewitz, "Local and global instabilities in spatially developing flows," Annu. Rev. Fluid Mech. **22**, 473 (1990).

[38]While closed flows can display convective instability, they generally do so over a limited parameter range before becoming absolutely unstable. See, for example, J. Fineberg, E. Moses, and V. Steinberg, "Spatially and temporally modulated traveling-wave pattern in convecting binary mixtures," Phys. Rev. Lett. **61**, 838 (1988); P. Kolodner and C. M. Surko, "Weakly nonlinear traveling-wave convection," *ibid.* **61**, 842 (1988); R. Tagg, W. S. Edwards, and H. L. Swinney, "Convective vs absolute instability in flow between counterrotating cylinders," Phys. Rev. A **42**, 831 (1990).

[39]R. J. Deissler, "The convective nature of instability in plane Poiseuille flow," Phys. Fluids **30**, 2303 (1987).

[40]In closed flows, even convectively unstable localized structures are confined by the boundaries; see, for example, J. Fineberg, V. Steinberg, and P. Kolodner, "Weakly nonlinear states as propagating fronts in convecting binary mixtures," Phys. Rev. A **41**, 5743 (1990).

[41]M. Nishioka and M. Asai, "Some observations of the subcritical transition in plane Poiseuille flow," J. Fluid Mech. **150**, 441 (1985).

[42]M. F. Schatz, R. P. Tagg, H. L. Swinney, P. F. Fischer, and A. T. Patera, "Supercritical transition in plane channel flow with spatially periodic perturbations," Phys. Rev. Lett. **66**, 1579 (1991).

[43]J. Guckenheimer and P. Holmes, *Nonlinear Oscillations, Dynamical Systems, and Bifurcations of Vector Fields* (Springer-Verlag, New York, 1983).

[44]J. H. Gerrard, "The wakes of cylindrical bluff bodies at low Reynolds numbers," Philos. Trans. R. Soc. London Ser. A **288**, 351 (1978).

[45]G. S. Triantafyllou, K. Kupfer, and A. Bers, "Absolute instabilities and self-sustained oscillations in the wakes of circular cylinders," Phys. Rev. Lett. **59**, 1914 (1987).

[46]J. M. Chomaz, P. Huerre, and L. G. Redekopp, "Bifurcations to local and global modes in spatially developing flows," Phys. Rev. Lett. **60**, 25 (1988).

[47]J. M. Chomaz, "Absolute and convective instabilities in nonlinear systems," Phys. Rev. Lett. **69**, 1931 (1992).

[48]B. J. Bayly, S. A. Orszag, and T. Herbert, "Instability mechanisms in shear-flow transition," Annu. Rev. Fluid Mech. **20**, 359 (1988).

[49]W. S. Saric, V. V. Kozlov, and V. Y. Levchenko, "Forced and unforced subharmonic resonance in boundary-layer transition," AIAA Paper No. AIAA-84-0007, 1984.

[50]T. Herbert, "Secondary instability of boundary layers," Annu. Rev. Fluid Mech. **20**, 487 (1988).

[51]M. F. Schatz and H. L. Swinney, "Secondary instability in plane channel flow with spatially periodic perturbations," Phys. Rev. Lett. **69**, 434 (1992).

[52]M. F. Schatz, "Transition in plane channel flow with spatially periodic perturbations," Ph.D. thesis, The University of Texas at Austin, 1991.

[53]For $n=1$, the two-dimensional spectral element mesh used in our calculations is shown in Fig. 2 of Ref. 10. For $n>1$, this mesh is repeated n times in the streamwise direction.

[54]Y. S. Kachanov and V. Y. Levchenko, "The resonant interaction of disturbances at laminar-turbulent transition in a boundary layer," J. Fluid Mech. **138**, 209 (1984).

[55]V. V. Kozlov and M. P. Ramazanov, "Development of finite-amplitude disturbances in Poiseuille flow," J. Fluid Mech. **147**, 149 (1984).

[56]R. J. Deissler, "Noise-sustained structure, intermittency, and the Ginzburg–Landau equation," J. Stat. Phys. **40**, 371 (1985).

[57]R. J. Deissler, "Spatially growing waves, intermittency and convective chaos in an open-flow system," Physica D **25**, 233 (1987).

[58]P. R. Fenstermacher, H. L. Swinney, and J. P. Gollub, "Dynamical instabilities and the transition to chaotic Taylor vortex flow," J. Fluid Mech. **94**, 103 (1979).

[59]W. S. Edwards (personal communication).